2-19-2018

From Intramolecular (Circular) in an Isolated Molecule to Intermolecular Hole Delocalization in a Two-Dimensional Solid-State Assembly: The Case of Pillarene

Maxim V. Ivanov
Marquette University

Denan Wang
Marquette University, denan.wang@marquette.edu

Tushar S. Navale
Marquette University

Sergey V. Lindeman
Marquette University, sergey.lindeman@marquette.edu

Rajendra Rathore
Marquette University

Accepted version. *Angewandte Chemie International Edition*, Vol. 57, No. 8 (February 19, 2018): 2144-2149. DOI.

Angewandte Chemie International Edition, Vol. 57, No. 8 (February 2018): 2144-2149. DOI.

From Intramolecular (Circular) in an Isolated Molecule to Intermolecular Hole Delocalization in a Two-Dimensional Solid-State Assembly: The Case of Pillarene

Dr. Maxim V. Ivanov
Department of Chemistry, Marquette University, Milwaukee, WI

Dr. Denan Wang
Department of Chemistry, Marquette University, Milwaukee, WI

Dr. Tushar S. Navale
Department of Chemistry, Marquette University, Milwaukee, WI

Dr. Sergey V. Lindeman
Department of Chemistry, Marquette University, Milwaukee, WI

Prof. Rajendra Rathore
Department of Chemistry, Marquette University, Milwaukee, WI

In memory of Jay K. Kochi

Abstract

To achieve long-range charge transport/separation and, in turn, bolster the efficiency of modern photovoltaic devices, new molecular scaffolds are needed that can self-assemble in two-dimensional (2D) arrays while maintaining both intra- and intermolecular electronic coupling. In an isolated molecule of pillarene, a single hole delocalizes intramolecularly via hopping amongst the circularly arrayed hydroquinone ether rings. The crystallization of pillarene cation radical produces a 2D self-assembly with three intermolecular dimeric (sandwich-like) contacts. Surprisingly, each pillarene in the crystal lattice bears a fractional formal charge of +1.5. This unusual stoichiometry of oxidized pillarene in crystals arises from effective charge distribution within the 2D array via an interplay of intra- and intermolecular electronic couplings. This important finding is expected to help advance the rational design of efficient solid-state materials for long-range charge transfer.

Keywords

2D assemblies, charge transfer, π-stacking, pillarenes

Funding Information

- Division of Chemistry. Grant Number: CHE-1508677
- National Heart, Lung, and Blood Institute. Grant Number: R01-HL112639-04

Article Text

The rational design of next-generation molecular scaffolds, which can self-assemble in two-dimensional arrays, is critically needed to achieve long-range charge transport/separation, which in turn can enhance the efficiency and performance of modern photovoltaic devices.[1-3] Importantly, such 2D architectures must allow both intra- and intermolecular electronic coupling.

The intramolecular stabilization of a single cationic charge (or hole) is well-known in cyclophane-like donors (**1**–**3**) featuring a pair of aromatic rings oriented over a range of inter-planar dihedral angles from 0° to 120°, as judged by the lowering of their oxidation potentials (350 to 250 mV) in comparison with the corresponding (monochromophoric) model compounds (Figure 1).[4] The hole stabilization in **1**–**3** (Figure 1) is also evidenced by the appearance of a new charge-resonance (or intervalence) transition in the electronic absorption spectra of their cation radicals (CRs). Crystallographic analysis of CRs **1**–**3** and their model compounds further demonstrates that the hole is delocalized over both aromatic rings as evidenced by the oxidation-induced structural reorganization (that is, contraction/elongation of the bond lengths), which is roughly one-half in $\mathbf{1}^{+\cdot}$–$\mathbf{3}^{+\cdot}$ of that found in the model CRs.

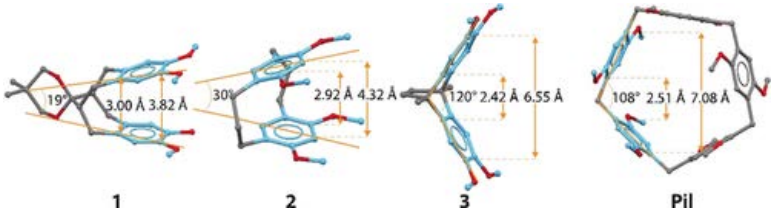

Figure 1. A comparison of the Pillarene (Pil) molecular structure (right) with a series of cyclophane-like electron donors **1**–**3** with varying interplanar angles. Lowering of E_{ox1} for **1**–**3** is 0.35, 0.35, 0.25 V, respectively.

Our continuing quest to identify efficient charge-transport materials, with recent focus on linear, cofacially arrayed, and cyclic poly-p-phenylene wires,[4-8] prompted us to examine if a single hole can be delocalized in pillar[5]arene (hereafter referred to as pillarene or Pil).[9-12]As shown in Figure 2, Pil is a cyclic (cofacial) array of

five p-hydroquinone ethers (p-HEs) separated by methylenes. Based on the X-ray structure of pillarene, the inter-planar dihedral angle is about 108° (Figure 2) and should thus afford modest through-space electronic coupling similar to that observed in ethanoanthracene (3, Figure 2) and triptycene derivatives.4 Indeed, we will show that pillarene forms a stable cation-radical salt both in solution and in the solid state. Surprisingly, we find that the circular (intramolecular) delocalization of the hole in Pil+. in solution is nearly halted in the solid state, where weak electronic coupling amongst the p-HE rings in Pil+. prompts the switching to intermolecular hole delocalization. Here, the optimal orbital overlap is achieved between the HOMOs of monomeric p-HE rings from different pillarene molecules. This unexpected modulation of the electronic structure of a cation radical from solution to solid state provide an important advance for the design of molecular scaffolds/assemblies for long-range charge transport via a combination of inter/intramolecular charge-transfer/stabilization mechanisms.

Pillarene can be easily accessed in excellent yield from a reaction of 1,4-dimethoxybenzene with paraformaldehyde in the presence of an acid.9 However, concerning the synthesis of pillarene, it is befitting to comment on prior work by Rathore and Kochi,13 who reported the preparation of a variety of diarylmethanes from benzyl methyl ethers. Therein, the transformation of a bis(methoxymethyl)-p-hydroquinone ether (1) to the corresponding diarylmethane (DAM) yielded as a side-product a polymer-like material from the electron-transfer or acid-catalyzed reactions (Scheme 1). Our re-analysis of this polymer, in the light of the reported synthesis of pillarene,9 shows that it consisted of largely (<80 %) pillarene, which can be purified by a simple crystallization from a CH2Cl2/acetonitrile mixture. The structure was confirmed by 1H/13C NMR spectroscopy, X-ray crystallography, and by comparison with an authentic sample.9

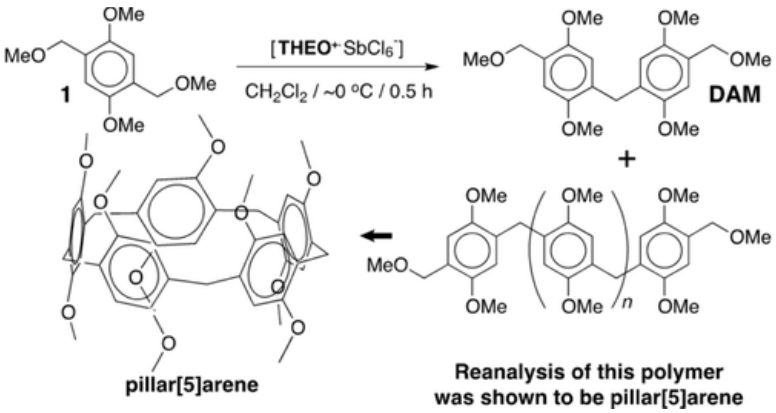

Scheme 1. Synthesis of pillarene, revisited from the work of Rathore and Kochi.13

To gauge the stability of Pil+., pillarene was subjected to cyclic voltammetric (CV) analysis. As shown in Figure 2 A, reversible electrochemical oxidation to form the cation radical (Eox1=0.58 V vs. Fc/Fc+) and dication (Eox2=0.72 V) was observed; however, upon removal of additional electrons, adsorption occurred at the electrode surface. The adsorption issues can be often overcome by employing an electrolyte containing non-coordinating bulky counter anions, for example, tetrakis(pentafluoro-phenyl)borate [TFAB−].14 Indeed, the cyclic voltammogram of pillarene with this electrolyte showed four reversible waves (at 0.53, 0.74, 1.10, and 1.44 V vs. Fc/Fc+) that correspond to the formation of cation radical, dication, trication, and tetracation, respectively,15 and without adsorption issues. Moreover, changing the electrolyte from [n-Bu4N+ PF6−] to [n-Bu4N+ TFAB−] increased the difference between Eox1/Eox2 of pillarene from 140 mV to 210 mV, owing to the reduced ion pairing.14 In turn, the polycation solubility is improved, reducing adsorption on the electrode surface.

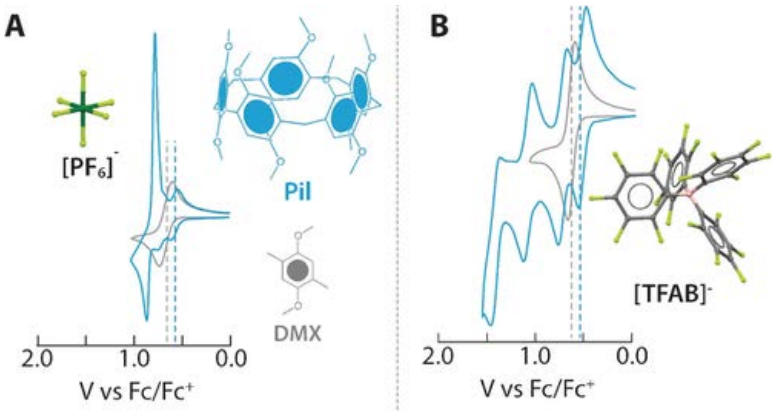

Figure 2. Cyclic voltammograms (CVs) of 2 mm Pil in the presence of 50 mm [n-Bu4N+ PF6−] as electrolyte (A) and in the presence of 50 mm [n-Bu4N+ TFAB−] with a bulky counter anion as electrolyte (B) at a scan rate of 200 mV s−1 in CH2Cl2 at 22 °C. CVs of model compound (DMX) are overlaid in gray.

In both cases, the first oxidation potential of pillarene was found to be about 80–90 mV lower than model 2,5-dimethoxy-p-xylene (DMX),[16] suggesting that electronic coupling amongst the circularly-arrayed p-HE rings is (relatively) weak as compared to the cyclophane-like donors 1–3 in Figure 3 (see below).

The cation radical of pillarene was generated in solution via (quantitative) redox titrations using [THEO+. SbCl6−] (Ered1=0.67 V vs. Fc/Fc+, λmax=518 nm, ϵmax=7300 L mol−1 cm−1) as an aromatic oxidant.[17] A quantitative deconvolution[18] of the component spectra of various species, present at each titration point in Figure 3 A, showed that upon addition of roughly 1 equiv of pillarene, the oxidant was largely consumed (see Figure S1 in the Supporting Information for details). A plot of the mole fractions of THEO+. and Pil+. against the added equivalents of Pil established a 1:1 stoichiometry of the redox reaction, that is, Pil0+THEO+.→Pil+.+THEO0 (Figure 3 B). It is noteworthy that the spectra of Pil+. remained unchanged at tenfold higher concentration, suggesting a lack of aggregation in solution.

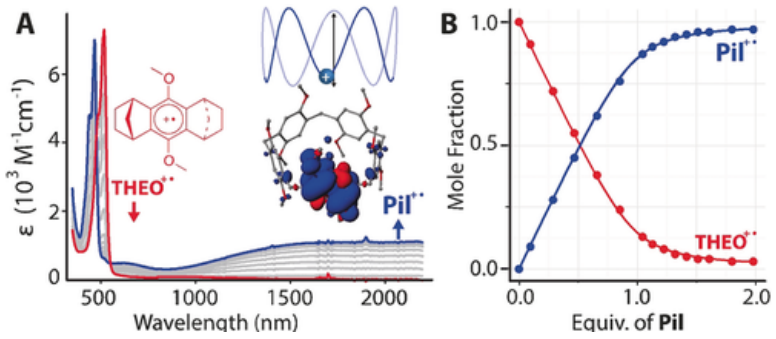

Figure 3. A) Spectral changes observed upon the reduction of 0.036 mM $THEO^{+\cdot}$ in CH_2Cl_2 (3 mL) by addition of 10 µL increments of 0.85 mM solution of Pil in CH_2Cl_2 at 22 °C. Inset: the isovalue plot of spin density distribution in $Pil^{+\cdot}$ and the NIR transition arising from hole hopping mechanism as represented by the Marcus-based multistate model.[7] B) Plot of the mole fractions of $THEO^{+\cdot}$ (red) and $Pil^{+\cdot}$ (blue) against the added equivalents of neutral Pil. Symbols represent experimental points, while the solid lines show best-fit to experimental points using $\Delta G_1 = E_{red}(THEO^{+\cdot}) - E_{ox1}(Pil) = 91$ mV.[18]

The absorption spectrum of $Pil^{+\cdot}$ (λ_{max}=467, 2000 nm; ϵ_{467}=7060, ϵ_{2000}=1100 L mol^{-1} cm^{-}), compared with model $DMX^{+\cdot}$ (λ_{max}=468 nm, ϵ_{468}=8100 L^{-1} mol cm^{-1}), showed a broad intervalence transition extending beyond 3000 nm. Such a transition reflects hole delocalization via through-space electronic coupling.[4] Indeed, the molar absorptivity of the intervalence transition in cofacially or circularly arrayed polychromophoric cation radicals has

been shown to correlate with the extent of electronic coupling.[19-21] Thus, the relatively low molar absorptivity of the intervalence transition in $Pil^{+\cdot}$ suggests a modest to weak electronic coupling amongst the circularly-arrayed *p*-HE rings, which should be contrasted with the intense near-IR absorption bands observed in various cofacially arrayed systems with larger overlap (**1**, **2**, and **3** in Figure 4).[4] The mechanism of hole distribution in such weakly coupled systems occurs via a hopping mechanism[12, 22, 23] that is also supported by DFT calculations and our recently developed Marcus-based multistate model[7] (see inset in Figure 4 A and Figure S21 in the Supporting Information).

Preparative isolation of pillarene cation radical was carried out by chemical oxidation using nitrosonium hexachloroantimonate as a 1 e^- oxidant. Thus, a 1:1 solution of pillarene and [NO^+ $SbCl_6^-$] in anhydrous CH_2Cl_2 was stirred under an argon atmosphere at about 0 °C, while bubbling argon through the solution to entrain gaseous nitric oxide. The resulting colored solution was carefully layered with toluene and stored in a refrigerator (−10 °C) for 2 days, which yielded single crystals suitable for X-ray crystallography. Crystals from two different crystallization attempts produced two nearly identical crystal structures albeit with somewhat different precisions, that is, averaged C−C bond length uncertainties (σ) of 1.82 pm and 0.54 pm (Figure S3 in the Supporting Information).

The crystal structure of $Pil^{+\cdot}$ revealed a highly unusual stoichiometry, where each pillarene moiety was associated with 1.5 equivalents of the $SbCl_6^-$ counteranion, indicating that pillarene bears 1.5 positive charges, that is, corresponding to an empirical formula=[$Pil^{1.5+\cdot}(SbCl_6^-)_{1.5}$] (Figure 4 A). A fractional charge is not feasible in an isolated single pillarene molecule in solution, but a formal fractional charge is perfectly viable within a crystal lattice, where it can arise from a crystallization-induced disproportionation. Interestingly, while a number of examples of crystallization-induced disproportionation of cation radicals to crystalline dications and neutral compounds has been observed,[16, 24] the disproportionation stoichiometry in the present case of the pillarene cation radical (that is, 3 $Pil^{+\cdot} \rightarrow 2\ Pil^{1.5+\cdot} + Pil^0$) is unusual and unprecedented.

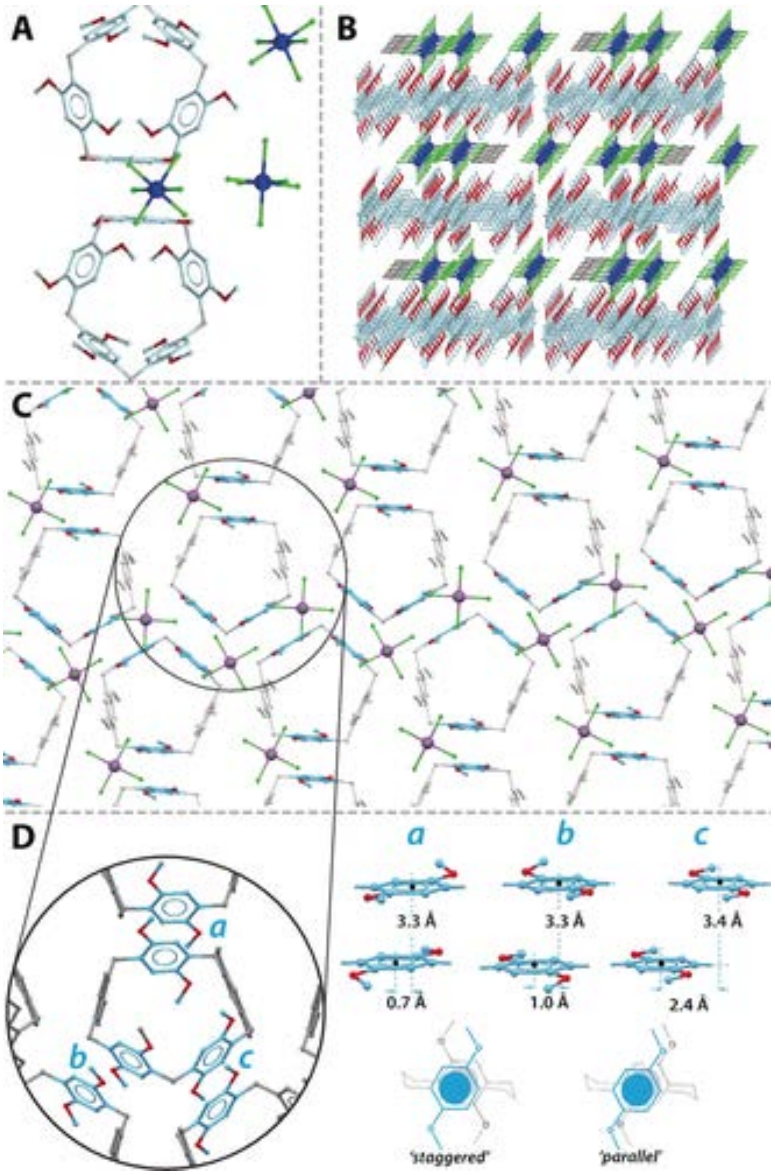

Figure 4. A) X-ray structure of [$Pil^{1.5+\cdot}$ $(SbCl_6^-)_{1.5}$] in a ball-and-stick model. B) Packing diagram showing alternating layers of pillarene molecules and $SbCl_6^-$ anions interlaced with toluene (gray) and disordered CH_2Cl_2 molecules (not shown). C) The crystal structure indicates that $SbCl_6^-$ counteranions are close to the dimeric contacts amongst two-dimensional array of cationic pillarenes. D) Structures of three dimers with interplanar distances and slippage. Staggered and parallel cyclophane donors are shown for comparison.

A closer look at the packing diagram of [$Pil^{1.5+\cdot}(SbCl_6^-)_{1.5}$] showed that it contains alternant layers of closely packed pillarene molecules and $SbCl_6^-$ anions together with solvent molecules, that is, toluene and disordered CH_2Cl_2 molecules (Figure 5 B). In the pillarene layer, three out of the five *p*-hydroquinone ether (*p*-HE) rings in each pillarene make a close (cofacial) sandwich-like contact with three other molecules, and thereby produce a continuous 2D array (Figure 5 C). This packing arrangement should be contrasted with numerous known9, 10, 25, 26 crystal structures of neutral pillarene which only show edge-to-face packing (for example, see Figure S4 in the Supporting Information). Furthermore, a close inspection of the three unique π-stacked sandwich-like pairs of *p*-HEs (identified as **a**, **b**, and **c** within the circle in Figure 5 D) in the 2D layer showed that each pair aligns as a parallel sandwich with interplanar separation of about 3.3 to 3.4 Å, which is shorter than the sum of the van der Waals contact. The slippage or extent of overlap in **a**–**c** varies, with **a**having optimal overlap (Figure 5 D). Importantly, the dimeric pairs **a**–**c** in the X-ray structure adopt a parallel arrangement of the

methoxy groups rather than the sterically less demanding staggered arrangement (Figure 5 D).[27] Such a conformational preference of the methoxy groups is not surprising in the light of the fact that the parallel dimers are expected to better stabilize a cationic charge (by ca. 140 mV) than their staggered diastereomer (Figure 5 D, bottom right).[28]

The packing diagram of [Pil$^{1.5+\cdot}$(SbCl$_6^-$)$_{1.5}$] suggests that the cationic charge must be largely concentrated at these dimeric units, and this notion is further supported by the positioning of SbCl$_6^-$ counteranions, which are located above these sandwich-like dimeric contacts (Figure 5 C). To quantify the extent of charge distribution in each *p*-HE ring in pillarene molecules in the [Pil$^{1.5+\cdot}$(SbCl$_6^-$)$_{1.5}$], we undertook a detailed analysis of the oxidation induced bond length changes in comparison with the neutral pillarene and the related model compounds.
It is well-established via X-ray crystallography that the oxidation-induced bond length changes can be used to establish the oxidation states of an aromatic hydrocarbon, that is, dication, cation radical or intervalence dimer cation radical where each unit bears 0.5 charge.[4, 16, 29] For example, we have recently shown[4, 30] with the aid of X-ray crystallography, electronic spectroscopy and DFT calculations in mono-, bi- and trichromophoric molecules (**V1**, **V2**, and **V3** in Figure 5 A) that the oxidation-induced bond length changes can be related directly to the amount of charge localized at each dimethoxybenzenoid (veratrole) unit, that is, bond length changes are smaller by a factor of two/three in **V2**$^{+\cdot}$/**V3**$^{+\cdot}$ as compared to model **V1**$^{+\cdot}$ (Figure 5 B).

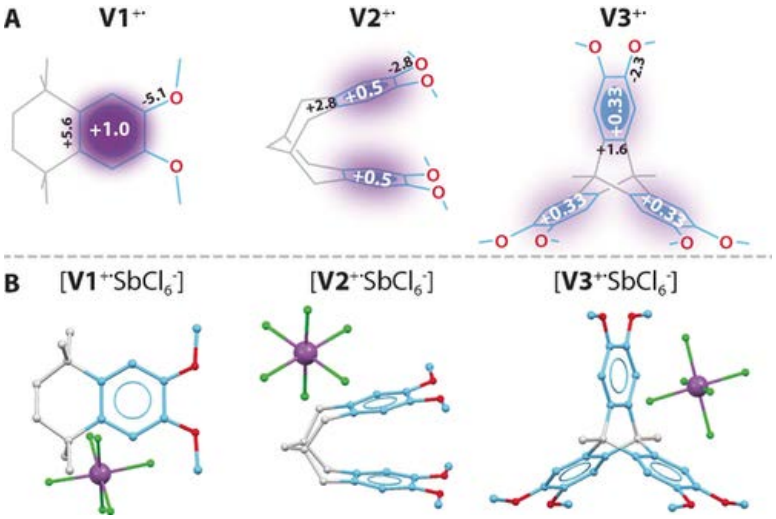

Figure 5. A) Structures of mono-, bi- and tri-chromophoric veratrole-based molecules (**V1**, **V2**, and **V3**) where hole distribution has been established by analysis of the oxidation-induced bond length changes (representative bond length changes are indicated) obtained from X-ray crystallography. B) X-ray structures of [**V1**$^{+\cdot}$SbCl$_6^-$], [**V2**$^{+\cdot}$SbCl$_6^-$], and [**V3**$^{+\cdot}$SbCl$_6^-$].

As a model compound for [Pil$^{1.5+\cdot}$(SbCl$_6^-$)$_{1.5}$], we employ a *p*-HE-based diarylethane (DAE) in neutral and cation radical states.[16] In solution, cationic charge in DAE$^{+\cdot}$ is localized on a single *p*-HE owing to the absence of the intramolecular electronic coupling between two *p*-HEs as established by electronic spectroscopy. In the solid state, however, the cofacial packing of *p*-HE rings leads to a redistribution of a single charge between two *p*-HEs within the dimeric contact (Figure 6 A). Remarkably, the interplanar distances and slippage between *p*-HEs in the dimeric contacts found in [Pil$^{1.5+\cdot}$(SbCl$_6^-$)$_{1.5}$] are uncannily similar to those found in the crystal structure of [DAE$^{+\cdot}$(SbCl$_6^-$)] (Figures 6 D and 6 A). A careful comparison of the bond length changes in various *p*-HE rings in [Pil$^{1.5+\cdot}$(SbCl$_6^-$)$_{1.5}$] (especially the contraction of C$_{Ar}$–O bonds) with that of the bond length changes in the *p*-HEs in model [DAE$^{+\cdot}$SbCl$_6^-$] showed that three of the five *p*-HE rings (that is, **a**, **b**, and **c**) in each pillarene (Figure 6 B) undergo bond length changes that are nearly identical to those found in the [DAE$^{+\cdot}$(SbCl$_6^-$)] crystal structure, consistent with each ring bearing approximately 0.5 cationic charge (see linear correlation plots in Figure 6 C). The remaining two *p*-HE rings (that is, **d** and **e**) show geometries similar to the neutral *p*-HE rings as indicated by absence of any correlation in Figure 6 C-d/e. Note that the bond length contractions/elongations in **a**, **b**,

and **c** follow the nodal arrangement of the HOMO of *p*-HE (that is, bonds with bonding lobes contract and bonds with antibonding lobes elongate; Figure 6 C) and are within the 3σ confidence level (Table S4 in the Supporting Information). An identical conclusion about the hole distribution in *p*-HEs **a**–**d** can be reached by comparing the bond length changes with other *p*-HE-based cation radicals and dications, for example, monochromophoric $DMX^{+\cdot}$ and a diarylpropane dication (DAP^{2+})29 (see the Supporting Information for a detailed analysis).

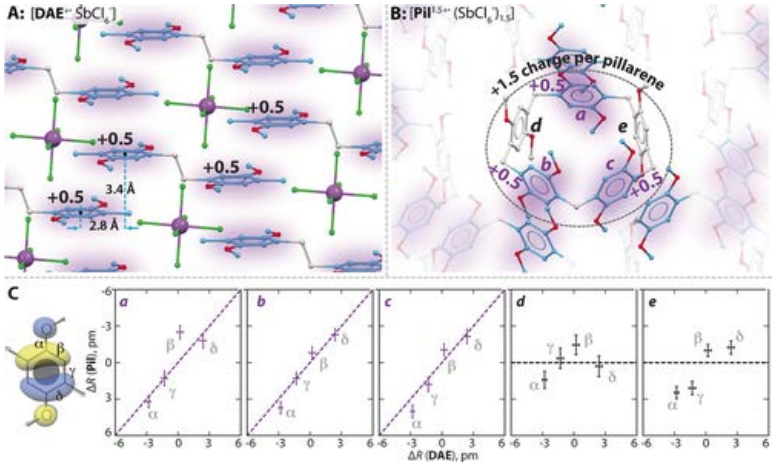

Figure 6. A) The packing diagram of [$DAE^{+\cdot}(SbCl_6^-)$] where a cationic charge is distributed evenly between two sandwiched *p*-HE rings. B) Two-dimensional arrangement of pillarene molecules in [$PIl^{1.5+\cdot}$ $(SbCl_6^-)_{1.5}$] and a close-up view of three intermolecular dimeric contacts. C) Correlation plots between the oxidation induced bond length changes in each *p*-HE unit of [$PIl^{1.5+\cdot}$ $(SbCl_6^-)_{1.5}$] plotted against the changes observed in *p*-HE rings in [$DAE^{+\cdot}(SbCl_6^-)$]. Uncertainties (*σ*) of individual bond length changes are shown as error bars.

Thus, each pillarene molecule in the X-ray structure of [$PIl^{1.5+\cdot}$ $(SbCl_6^-)_{1.5}$] is involved in the formation of three intermolecular dimeric cation radicals with sandwich-like geometries, and each *p*-HE ring in these dimers bears 0.5 charge. This analysis thus clearly accounts for the formal 1.5 charge per pillarene unit in the X-ray structure of [$PIl^{1.5+\cdot}$ $(SbCl_6^-)_{1.5}$], and may also provide a mechanistic path for the effective charge delocalization/hopping within the 2D-array by a combination of intra-/intermolecular electronic couplings. Moreover, this structural analysis further suggests that crystalline [$PIl^{1.5+\cdot}$ $(SbCl_6^-)_{1.5}$] should show an intense intervalence transition in the solid state as found in the solid state of [$DAE^{+\cdot}(SbCl_6^-)$].16 Indeed, a diffuse reflectance spectrum of crystalline [$PIl^{1.5+\cdot}(SbCl_6^-)_{1.5}$] shows an intense blue-shifted transition (1500 nm in solid vs. >2000 nm in solution) which has a molar absorptivity by a factor of three higher than the solution spectrum of $PIl^{+\cdot}$ (see Figure S2 in the Supporting Information).

On the one hand, a drastic difference in the hole delocalization of isolated pillarene in solution as compared to the extended pillarene network in the solid state is not surprising given the fact that a cofacial arrangement of *p*-HE rings between two adjacent pillarenes provides a strong intermolecular coupling, while the intramolecular electronic coupling in an isolated pillarene must be relatively small. Based on our recent study with triptycene derivatives,30 the intramolecular electronic coupling amongst *p*-HE rings in isolated pillarene can be estimated using Hückel molecular orbital theory (HMO), where the filled molecular orbitals (FMOs) of pillarene result from a linear combination of HOMOs of the *p*-HE rings (that is, coarse-grained HMO).31 Because pillarene has a circular topology with five nodes, the energies of its five highest occupied molecular orbitals can be obtained from an inverted Frost circle method, which directly provides the electronic coupling *β*: that is, $\Delta = 3.618\,\beta$, where *Δ* is splitting between HOMO and HOMO−4 (Figure 7 A).32 Using the energies of the five HOMOs of pillarene obtained by DFT calculations [B1LYP-40/6-31G(d)+PCM(CH_2Cl_2)]33 in the inverted Frost circle in Figure 7 A, we obtain a value of $\beta = 83$ mV.

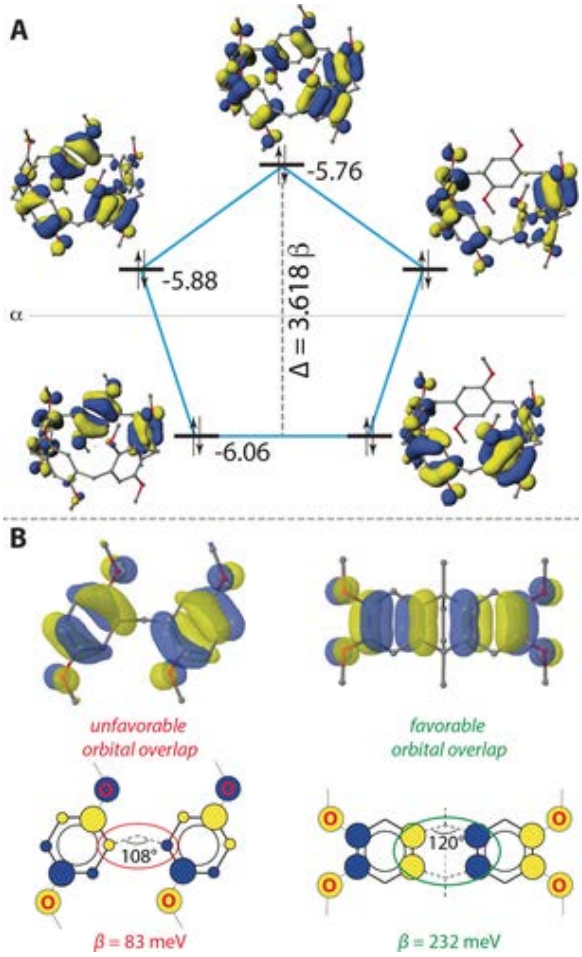

Figure 7. A) Inverted Frost circle diagram of five highest occupied MOs of pillarene obtained from DFT calculations. B) The reduced orbital overlap in Pil as compared to **3** owing to reduced HOMO density at the carbons in Pil in the region of interchromophoric coupling.

The modest intramolecular *β* value in isolated pillarene predicted via the Hückel method is consistent with a modest lowering of its E_{ox1} and low molar absorptivity of the intervalence transition in its cation radical (Figure 8). As such, the reduced electronic coupling amongst the *p*-HE rings in pillarene, despite a favorable interplanar angle (ca. 108°, *β*=83 meV) as compared to **3** or related triptycene derivatives (ca. 120°, *β*=230–280 meV, Figure 8 B), arises from the shapes of the HOMOs of *p*-HEs, which render the HOMO density to be relatively small in the region of the interchromophoric interaction. This is in contrast to the sandwich-like arrangement of *p*-HE rings in crystals, where the orbital overlap is expected to be optimal (*β*≈340 meV).[34] Note that interchromophoric electronic coupling can be diminished or eliminated owing to unfavorable nodal arrangement of interacting HOMOs of chromophores, despite a favorable geometrical orientation.[30]

The hole delocalization amongst the circularly arrayed *p*-HEs in pillarene cation radical in solution is demonstrated by the electronic spectroscopy and the lowering of its E_{ox1}. However, owing to a modest interchromophoric electronic coupling in pillarene arising from the unfavorable nodal arrangement of the interacting HOMOs of *p*-HEs,[30] the (circular) intramolecular hole delocalization in solution is diminished in the solid state assembly in the favor of the formation of three intermolecular dimeric cation radicals with sandwich-like geometries, which allow effective stabilization of cationic charges.[35] This is to be contrasted with other cyclophane-like donors (Figure 8), which show complete hole delocalization both in solution and solid-state because of the large electronic coupling (Figure 8 B). Furthermore, we also note that numerous crystal structures of neutral pillarene[9, 10, 25, 26] only show edge-to-face packing, while oxidized pillarene packs in

two-dimensional π-stacked arrays (Figure S4 in the Supporting Information), which could provide a conduit for long-range charge transfer.

This unusual finding of crystallization-induced alteration of the electronic structure of pillarene cation radical and its tight packing via π-stacking introduces an important new criterion for the design of next-generation molecular assemblies that may hold potential to achieve long-range charge transport via a combination of inter-/intramolecular charge transfer.

Acknowledgements

We thank NSF (CHE-1508677) and NIH (R01-HL112639-04) for financial support, Professors Scott A. Reid and Marat R. Talipov for helpful discussions and Professor William E. Geiger (University of Vermont) for kindly supplying us with a sample of bulky electrolyte [*n*-$Bu_4N^+TFAB^-$]. Calculations were performed on Père (MU) and XSEDE (NSF) computing clusters.

Conflict of Interest

The authors declare no conflict of interest.

Supporting Information

From Intramolecular (Circular) in an Isolated Molecule to Intermolecular Hole Delocalization in a Two-Dimensional Solid-State Assembly: The Case of Pillarene

Maxim V. Ivanov, Denan Wang, Tushar S. Navale, Sergey V. Lindeman, and Rajendra Rathore*

Department of Chemistry Marquette University, Milwaukee, WI

ELECTRONIC SPECTROSCOPY OF PILLAR[5]ARENE (PILLARENE) CATION RADICAL

Generation of pillarene cation radical in solution

Reproducible cation radical spectra of pillar[5]arene (hereafter referred to as pillarene or **Pil**) were obtained by quantitative redox titrations1,2 using [**THEO**+•SbCl6–]3 (*E*red1 = 0.67 V vs Fc/Fc+, λmax = 518 nm, εmax = 7300 cm-1 M-1) as an aromatic oxidant. The redox titrations were performed at 22 °C by an incremental addition of a solution of 0.85 mM of **Pil** in CH2Cl2 to a 0.036 mM solution of [**THEO**+•SbCl6–] in CH2Cl2. Resulting absorption spectra (Figure S1A) were numerically deconvoluted at each increment,1 providing the spectra of **Pil**+• (Figure S1B) and **THEO**+• (Figure S1C) at each titration point or at the addition of each increment of **Pil.** This deconvolution procedure1 provided the mole fractions of each species against the added equivalents of **Pil** at each titration point that confirmed a 1:1 stoichiometry of the redox reaction: **THEO**+• + **Pil** ⇄ **THEO** + **Pil**+• (Figure S1D).

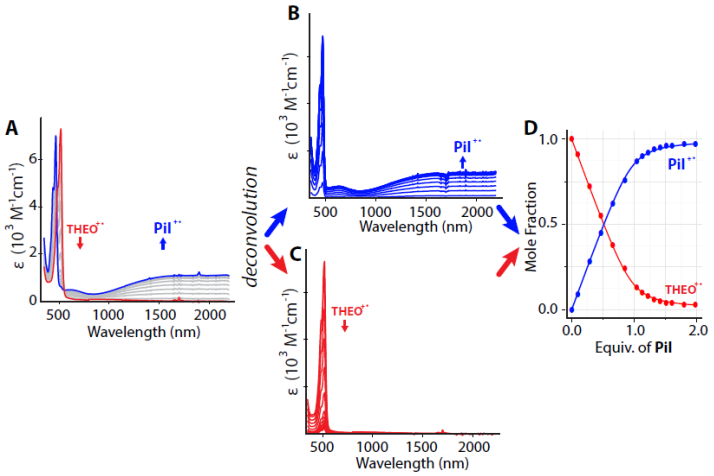

Figure S1. A: Spectral changes observed upon the reduction of 0.036 mM **THEO**$_{+\bullet}$ in CH_2Cl_2 (3 mL) by addition of 10-µL increments of 0.85 mM solution of **Pil** in CH_2Cl_2. B, C: Showing clean deconvolution of each spectrum from panel A into its component spectra, i.e. **Pil**$_{+\bullet}$ (blue, B) and **THEO**$_{+\bullet}$ (red, C). D: Plot of the mole fractions of **THEO**$_{+\bullet}$ (red) and **Pil**$_{+\bullet}$ (blue) against the added equivalents of neutral **Pil**. Symbols represent experimental points, while the solid lines show best-fit to experimental points using $\Delta G_1 = E_{red}(\mathbf{THEO}_{+\bullet}) - E_{ox1}(\mathbf{Pil}) = +91$ mV.[1,2]

Solid-state diffuse reflectance spectroscopy of crystalline [Pil$_{1.5+\bullet}$(SbCl$_{6-}$)$_{1.5}$]

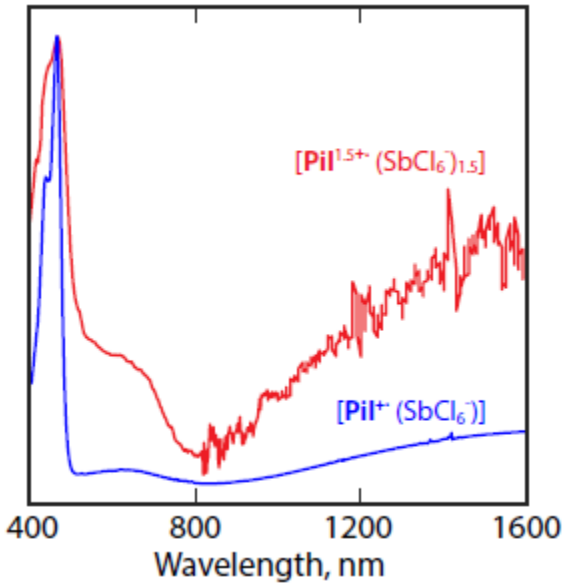

Figure S2. Normalized diffuse reflectance spectrum of crystalline [**Pil**$_{1.5+\bullet}$(SbCl$_{6-}$)$_{1.5}$] in solid state is compared with the solution spectrum of [**Pil**$_{+\bullet}$SbCl$_{6-}$] in CH_2Cl_2. Intensity of the high energy local band was used to normalize spectra. Note that same batch of crystals were used for the determination of X-ray structure presented in the manuscript as well as for the recording of diffuse-reflectance spectrum presented above.

Additional packing diagrams of [Pil$_{1.5+\bullet}$(SbCl$_{6-}$)$_{1.5}$] and comparison with neutral pillarene

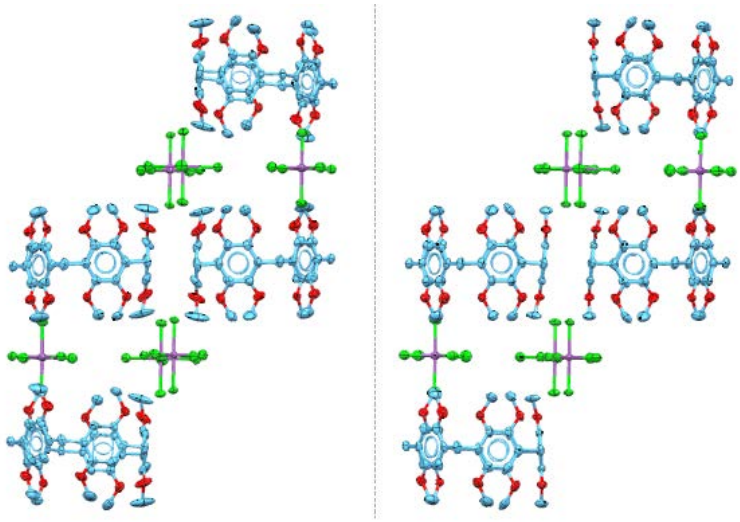

Figure S3. ORTEP diagram (50% probability) of two [**Pil**1.5+•(SbCl6-)1.5] crystal structures, i.e., raj13ka (left) and raj28b (right) showing identical packing arrangement of pillarene molecules and SbCl6- counter anions. Disordered solvent molecules are excluded for clarity.

Note: Numerous known crystal structures of neutral pillarene only show edge-to-face packing (left),[4-7] while oxidized pillarene packs in two-dimensional π-stacked arrays (right).

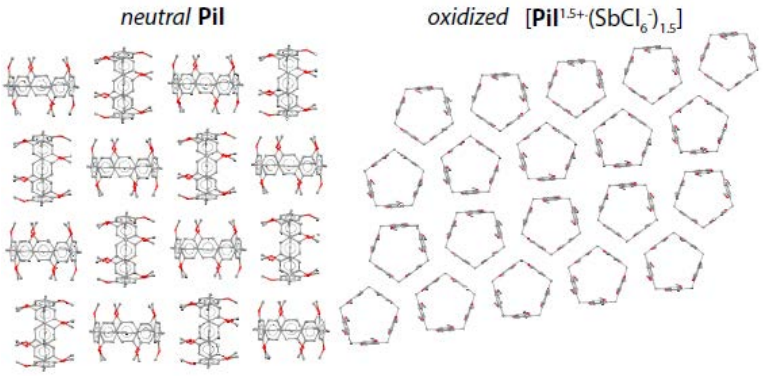

Figure S4. Comparison of the packing of pillarene molecules in the crystal structures of neutral (left) and oxidized (right) states. Neutral pillarenes form edge-to-face contacts between aromatic *p*-HE rings and methyl groups (via C-H–π interactions), while oxidized pillarenes form π-stacking between *p*-HE units.

DESCRIPTION OF HOLE DISTRIBUTION VIA ANALYSIS OF THE OXIDATIONINDUCED BOND LENGTH CHANGES IN THE X-RAY STRUCTURES OF PILLARENE AND VARIOUS MODEL COMPOUNDS

Analysis of the oxidation-induced bond length changes, determined by comparison of the X-ray crystals structures of neutral/oxidized aromatic hydrocarbons, can be effectively utilized to establish its oxidation states, i.e., dications, cation radicals or intervalence dimer cation radicals where each unit bears 0.5 charge.[8-11]

For example, we have recently shown with the aid of X-ray crystallography, electronic spectroscopy, and DFT calculations that a single cationic charge is evenly distributed between 1,2- dimethoxybenzenoid units in bi- and tri-chromophoric molecules when compared with monochromophoric model compound (see, structure **V1**, **V2**, and **V3** in Figure S5A).[8-11] Analysis of the precise X-ray crystal structures of neutral **V1**, **V2**, **V3** and their cation radicals (Figure S5A/B) clearly showed that oxidation-induced bond length changes are directly related to the amount of charge localized at each benzenoid unit, i.e., bond length changes vary by a factor of two/three smaller in **V2**$^{+\bullet}$/**V3**$^{+\bullet}$ as compared to changes in model **V1**$^{+\bullet}$. Moreover, DFT calculations using an extensively

calibrated density functional[12] well reproduced the electronic structure of **V1**$^{+\bullet}$, **V2**$^{+\bullet}$ and **V3**$^{+\bullet}$ obtained by X-ray crystallography (compare Figures S5B and S5C).

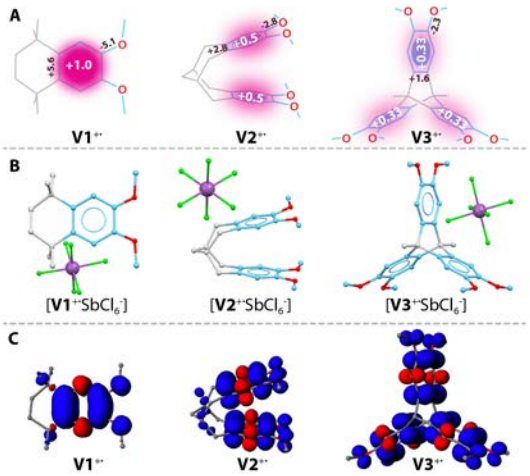

Figure S5. A. Structures of mono- (**V1**), di- (**V2**) and tri-chromophoric (**V3**) molecules. B. ORTEP diagrams of [**V1**$^{+\bullet}$$SbCl_6^-$], [**V2**$^{+\bullet}$$SbCl_6^-$] and [**V3**$^{+\bullet}$$SbCl_6^-$] X-ray crystal structures. C. Isovalue spin-density plots of **V1**$^{+\bullet}$, **V2**$^{+\bullet}$ and **V3**$^{+\bullet}$ obtained from DFT calculations using [B1LYP-40/6-31G(d)+PCM(CH_2Cl_2)].[12]

Unlike [**V1**$^{+\bullet}$$SbCl_6^-$], [**V2**$^{+\bullet}$$SbCl_6^-$] and [**V3**$^{+\bullet}$$SbCl_6^-$] where single cationic charge is distributed over 1, 2, and 3 benzenoid rings, respectively, we note that the in crystal structure of [**Pil**$_{1.5}^{+\bullet}$ ($SbCl_6^-$)$_{1.5}$], reported herein, has a highly unusual stoichiometry, where each pillarene moiety is associated with 1.5 equivalents of $SbCl_6^-$ counteranion, indicating that it must bear fractional 1.5 positive charges.

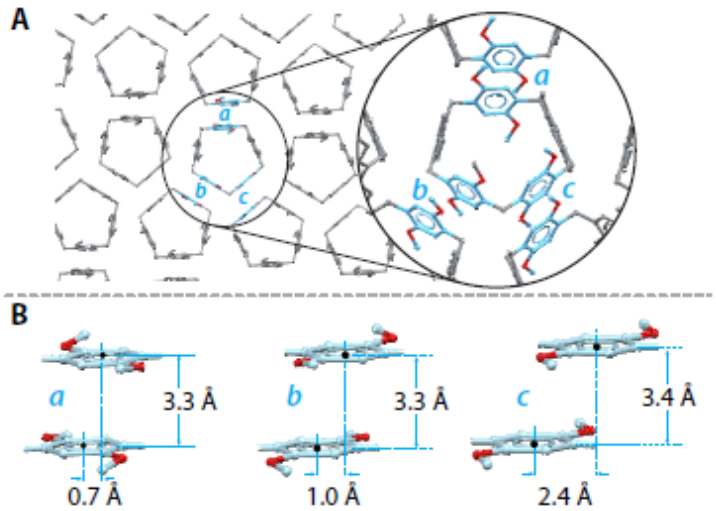

Figure S6. A. Two-dimensional arrangement of pillarene molecules within a layer and a zoomed-in view of three intermolecular dimeric contacts. B. Structures of three dimers with interplanar distances and slippage.

Each pillarene molecule in [**Pil**$_{1.5}^{+\bullet}$ ($SbCl_6^-$)$_{1.5}$] has five unique *para*-hydroquinone ether (i.e., *p*-HE) rings with varied degree of cofacial sandwich-like contact with *p*-HE rings of the adjacent pillarene molecules within the continuous 2D array. Among five units, three *p*-HE pairs (identified as **a**, **b**, and **c** in the circle in Figure S6A) have an optimal cofacial sandwich-like overlap with *p*-HE rings of the adjacent pillarene molecules with an interplanar separation of ~3.3 to 3.4 A, which is shorter than the sum of the van der Waals contact (3.5 A).

Herein, we will demonstrate using strategies akin to those employed in Figure S5 that the analysis of the bond length changes within each *p*-HE unit in [**Pil**$_{1.5+\bullet}$ ($SbCl_{6-}$)$_{1.5}$] can be used to establish the amount of charge on each *p*-HE ring with the aid of *p*-HE-based model compounds shown below (Figure S7).

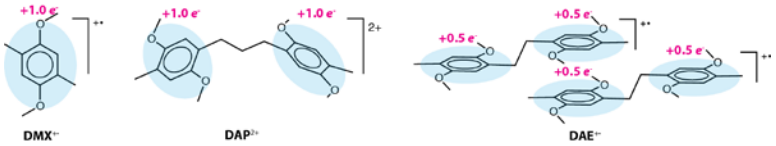

Figure S7. Structures of *p*-HE-based model compounds employed for comparison with the oxidation-induced bond length changes in [**Pil**$_{1.5+\bullet}$ ($SbCl_{6-}$)$_{1.5}$].

For example, we have shown that the scrutiny of the oxidation-induced bond length changes in **DMX**$_{+\bullet}$, **DAP**$_{2+}$ and **DAE**$_{+\bullet}$ (Figure S7) allows one to quickly discern the oxidation state of their *p*-HE units, i.e., in **DAP**$_{2+}$, each *p*-HE units bear +1.0 charge, while in **DAE**$_{+\bullet}$, dimer cation radical like packing renders each *p*-HE unit to bear only +0.5 charge.[9] Availability of these precise X-ray structures of *p*-HE-based model compounds with +1 and +0.5 oxidation states provides a foundational basis to show that bond length changes can be utilized to establish the oxidation states of each *p*-HE unit in a complex polychromophoric molecule, such as [**Pil**$_{1.5+\bullet}$ ($SbCl_{6-}$)$_{1.5}$].

Although the model compounds **DMX**$_{+\bullet}$, **DAP**$_{2+}$ and **DAE**$_{+\bullet}$ have been described in detail earlier,[8-11] below we provide a brief description of each of these structures together with the analysis of the bond length changes employed for establishing their oxidation states for the sake of maintaining the continuity of the description of the methodology. Such a description is necessary as it provide the context of the usage of these model compounds as an aid to analyze the oxidation state of each *p*-HE unit in [**Pil**$_{1.5+\bullet}$ ($SbCl_{6-}$)$_{1.5}$] crystal structure.

*2,5-dimethoxy-p-xylene crystal structures (i.e., **DMX/DMX**$_{+\bullet}$)*

The crystal structures of neutral **DMX** and its cation radical [**DMX**$_{+\bullet}$$SbCl_{6-}$] showed that they both pack **as** well-separated molecules with the center-to-center distance between aromatic rings of 7-8 A (Figure S8), which is far beyond the sum of van der Waals radii. As such the packing arrangements displayed in Figure S8 demonstrate the absence of any dimeric contacts and therefore, in [**DMX**$_{+\bullet}$$SbCl_{6-}$] entire cationic charge resides on the single **DMX**$_{+\bullet}$ molecule.

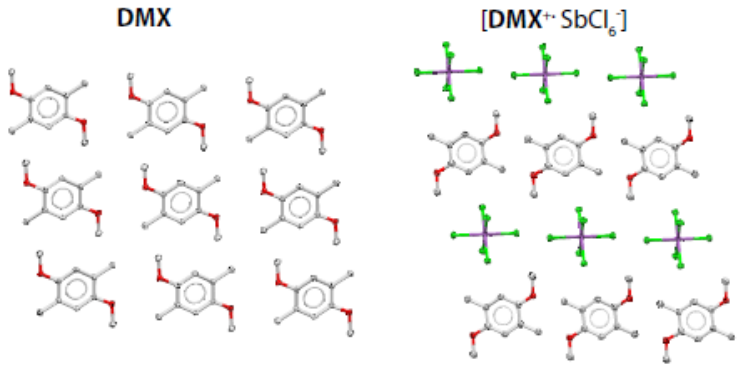

Figure S8. Packing diagrams of **DMX** and [**DMX**$_{+\bullet}$$SbCl_{6-}$]

Comparison of the crystal structures of neutral **DMX** and [**DMX**$_{+\bullet}$$SbCl_{6-}$] showed that upon oxidation it exhibits significant bond length changes that collectively can be referred to as a quinoidal distortion (see structures in Table S1). In particular, the aromatic C-C bonds 'δ' and 'β' undergo elongation by 3.4 pm and 0.9 pm, respectively, while C-C bond 'δ' contracts by 2.9 pm. Importantly, C_{Ar}-O bond ('α') undergoes most prominent change, i.e, it shortes by 5.2 pm. Due to the high precision of both neutral and cation radical structures of **DMX**, all bond length changes satisfy the commonly applied 3σ confidence level (see Table S1).

Table S1. Comparison of the bond lengths (pm) and their uncertainties (pm) in **DMX**/**DMX**$^{+\bullet}$. Equivalent bonds are averaged. Uncertainty of the oxidation-induced bond length changes was obtained as the sum of normally distributed variables, i.e., $\sigma = \sigma_2(\mathbf{DMX}) + \sigma_2(\mathbf{DMX}^{+\bullet})$.

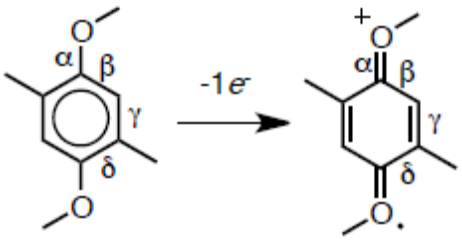

	α	β	γ	δ	Average σ
DMX	138.0(1)	139.4(1)	139.6(1)	140.1(1)	0.1
$DMX^{+\bullet}$	132.8(3)	140.3(3)	136.7(3)	143.5(3)	0.3
$\Delta R(DMX^{+\bullet})$	-5.2(3)	0.9(3)	-2.9(3)	3.4(3)	0.3

Electronic structure of **DMX**/**DMX**$^{+\bullet}$ discerned by the X-ray crystallography is fully reproduced by the DFT calculations at B1LYP-40/6-31G(d) level of theory, which was extensively calibrated to reproduce electronic structure of various π-conjugated cation radicals.[12-15] A correlation plot between oxidation-induced bond length changes obtained from DFT calculations and those obtained from X-ray crystallography shows a perfect linear dependence (Figure S9). Importantly, bond length changes upon **DMX**→**DMX**$^{+\bullet}$ transformation track in accordance with the nodal arrangement of HOMO in **DMX**, i.e., bonds with bonding HOMO lobes undergo elongations, and bonds with antibonding HOMO lobes undergo contractions (Figure S9).

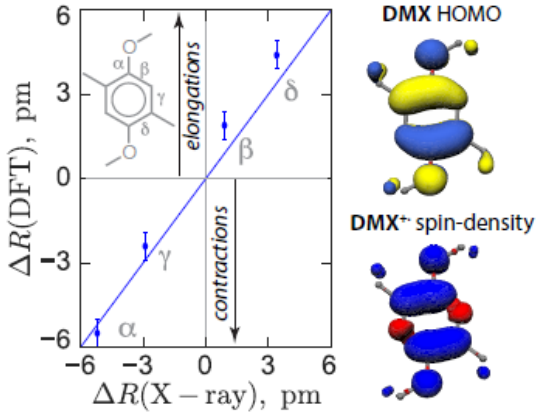

Figure S9. Correlation plot of bond length changes upon **DMX**→**DMX**$^{+\bullet}$ transformation obtained from DFT and X-ray crystallography

*Diarylpropane crystal structures (i.e., **DAP**/**DAP**$^{2+}$)*

Crystal structures of both neutral **DAP** and its dication [**DAP**$^{2+}$(SbCl$_6^-$)$_2$] showed two well separated structurally equivalent *p*-HE units (Figure S10). In [**DAP**$^{2+}$(SbCl$_6^-$)$_2$], all *p*-HE contacts exceed the sum of the van der Waals radii, suggesting that each aryl group bears +1.0 charge.

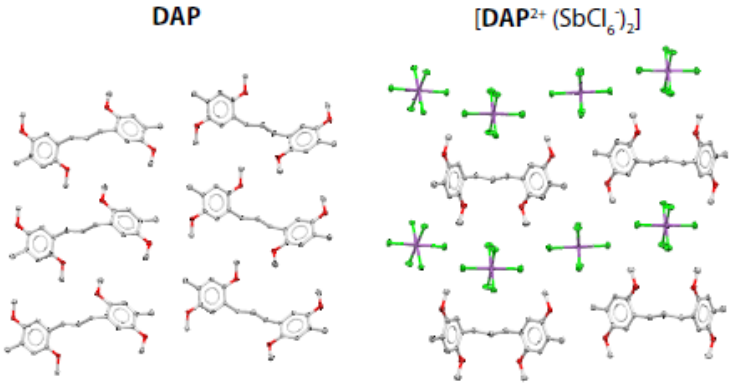

Figure S10. Packing of **DAP** and [**DAP**$^{2+}$(SbCl$_6$)2]

Comparison of the **DAP** and [**DAP**$_{2+}$(SbCl$_6$)$_2$] crystal structures showed that upon oxidation, each *p*-HE unit in **DAP** undergoes oxidation-induced quinoidal distortion that is similar to that found in **DMX**→**DMX**$_{+\bullet}$ transformation (Table S2). For example, C$_{Ar}$-O bond (i.e., 'α') in each *p*-HE unit of **DAP**$_{2+}$ underwent a significant shortening of 4.9 pm that is identical (within the uncertainty) to that found in **DMX**$_{+\bullet}$ (Table S2).

Table S2. Comparison of the bond lengths (pm) and their uncertainties (pm) in **DAP**/**DAP**$_{2+}$. Equivalent bonds are averaged. Uncertainty of the oxidation-induced bond length changes was obtained as the sum of normally distributed variables, i.e., $\boldsymbol{\sigma} = \boldsymbol{\sigma}_2(\mathbf{DAP}) + \boldsymbol{\sigma}_2(\mathbf{DAP}_{2+})$.

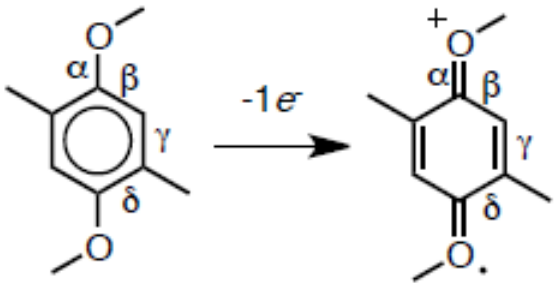

	α	β	γ	δ	Average σ
DAP	137.5(1)	139.5(2)	139.7(2)	140.0(2)	0.2
DAP2+	132.7(4)	140.8(4)	137.2(5)	144.7(5)	0.5
ΔR(DAP2+)	-4.9(4)	1.2(4)	-2.5(5)	4.8(5)	0.5
ΔR(DMX+•)	-5.2(3)	0.9(3)	-2.9(3)	3.4(3)	0.3

In fact, all bond length changes that occur upon **DAP**→**DAP**$_{2+}$ transformation are nearly identical to those observed in **DMX**→**DMX**$_{+\bullet}$ transformation (Table S2). Indeed, a correlation plot between bond length changes in **DMX**$_{+\bullet}$ and **DAP**$_{2+}$ for all four bonds shows a clear linear dependence (Figure S11) with expected unity slope. Only a single bond (i.e., 'δ') shows a minor deviation from the perfect linear line (Figure S11), which should not be surprising as these bond length changes were obtained from different crystal structures with varied packing and relative positions of the counter anions. Nevertheless, despite these differences, a simple comparative analysis of the oxidation-induced bond length changes allows one to quickly discern the oxidation state of *p*-HE units in [**DMX**$_{+\bullet}$SbCl$_6$] and [**DAP**$_{2+}$(SbCl$_6$)$_2$].

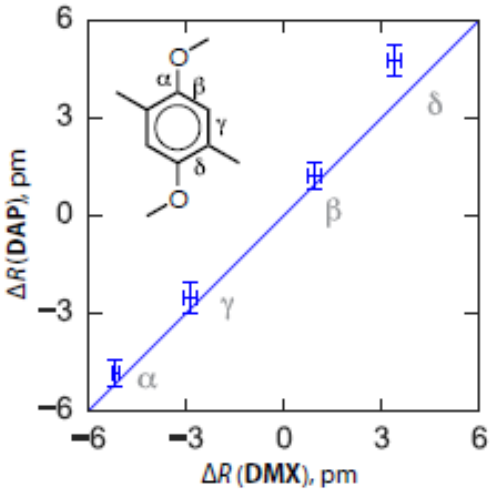

Figure S11. Correlation plot between oxidation-induced bond length changes in *p*-HE units of $\mathbf{DAP}^{2+}$ and those of $\mathbf{DMX}^{+\bullet}$. Equivalent bonds are averaged. Uncertainties (σ) of individual bond length changes are shown as error bars.

*Diarylethane crystal structures (i.e., **DAE/DAE**$^{+\bullet}$)*

The crystal structure of [$\mathbf{DAE}^{+\bullet}SbCl_6^-$] showed that $\mathbf{DAE}^{+\bullet}$ molecules pi-stack along the *x*-axis and form dimeric van der Waals contacts between *p*-HE units of adjacent $\mathbf{DAE}^{+\bullet}$ with the interplanar separation of ~3.4 A (Figure S12). Because *p*-HE units in each $\mathbf{DAE}^{+\bullet}$ are symmetrically equivalent, cationic charge is evenly delocalized between two *p*-HEs in $\mathbf{DAE}^{+\bullet}$, i.e. that each *p*-HE in $\mathbf{DAE}^{+\bullet}$ bears +0.5 charge.

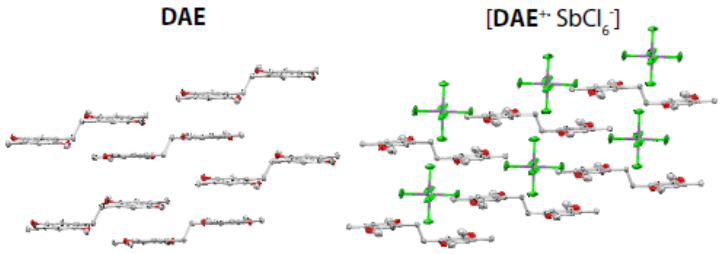

Figure S12. Packing diagrams of **DAE** and [$\mathbf{DAE}^{+\bullet}SbCl_6^-$]

Furthermore, diffuse-reflectance absorption spectrum of the [$\mathbf{DAE}^{+\bullet}SbCl_6^-$] crystals showed an intervalence near-IR transition, confirming an effective through-space hole delocalization within dimeric contacts.[9] Comparison of the **DAE** and [$\mathbf{DAE}^{+\bullet}(SbCl_6^-)_2$] crystal structures showed that upon oxidation, each *p*-HE unit in **DAE** undergoes quinoidal distortion that is similar to that in $\mathbf{DMX}\rightarrow\mathbf{DMX}^{+\bullet}$ transformation (Table S3). However, the magnitude of these changes was found to be smaller by a factor of two than those observed in **DMX** (Table S3). For example, C_{Ar}-O bond (i.e., 'α') in each *p*-HE unit of $\mathbf{DAE}^{+\bullet}$ underwent a shortening of 2.8 pm as compared to 5.2 pm shortening found in $\mathbf{DMX}^{+\bullet}$ (Table S3).

Table S3. Comparison of the bond lengths (pm) and their uncertainties (pm) in $\mathbf{DAE}/\mathbf{DAE}^{+\bullet}$. Equivalent bonds are averaged. Uncertainty of the oxidation-induced bond length changes was obtained as the sum of normally distributed variables, i.e., $\boldsymbol{\sigma} = \boldsymbol{\sigma}^2(\mathbf{DAE}) + \boldsymbol{\sigma}^2(\mathbf{DAE}^{+\bullet})$.

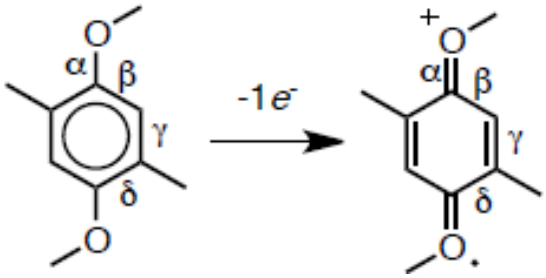

	α	β	γ	δ	Average σ
DAE	137.7(1)	139.2(1)	139.5(1)	139.9(1)	0.1
DAE$^{+\bullet}$	134.9(2)	139.4(3)	138.3(3)	142.3(3)	0.3
Δ*R*(**DAE**$^{+\bullet}$)	-2.8(2)	0.2(3)	-1.3(3)	2.4(3)	0.3
Δ*R*(**DMX**$^{+\bullet}$)	-5.2(3)	0.9(3)	-2.9(3)	3.4(3)	0.3

Indeed, a correlation plot between bond length changes in **DMX**$^{+\bullet}$ and **DAE**$^{+\bullet}$ for all four bonds showed a clear linear relation with the slope of 0.5 (Figure S14). Expectedly, a similar correlation plot between **DMX**$^{+\bullet}$ and **DAP**$^{2+}$ also showed the same 0.5 value of the slope (Figure S14).

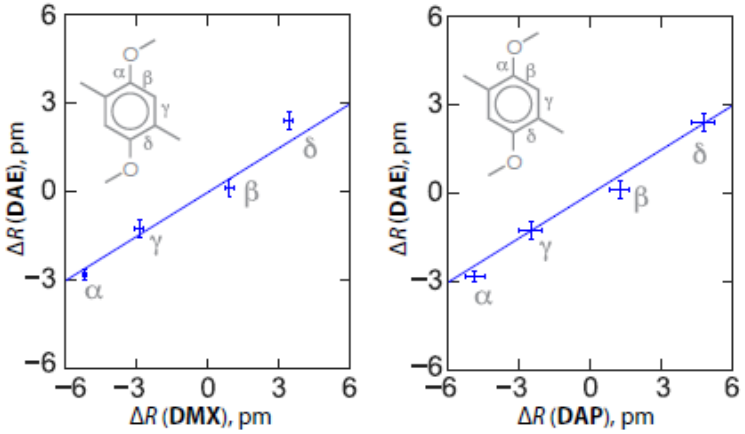

Figure S13. Correlation plot between oxidation-induced bond length changes in *p*-HE units of **DAE**$^{+\bullet}$ and those of **DMX**$^{+\bullet}$ (left) and **DAP**$^{2+}$ (right). Equivalent bonds are averaged. Uncertainties (σ) of individual bond length changes are shown as error bars.

The analysis presented above clearly demonstrated the underpinnings of the oxidation-induced bond length changes in aromatic hydrocarbons on the example of *p*-HE-based derivatives, i.e., the bonds' elongation/contractions are defined by the nodal arrangement of the HOMO (Figure S9), while the extent of these changes is proportional to the amount of charge at the given *p*-HE.

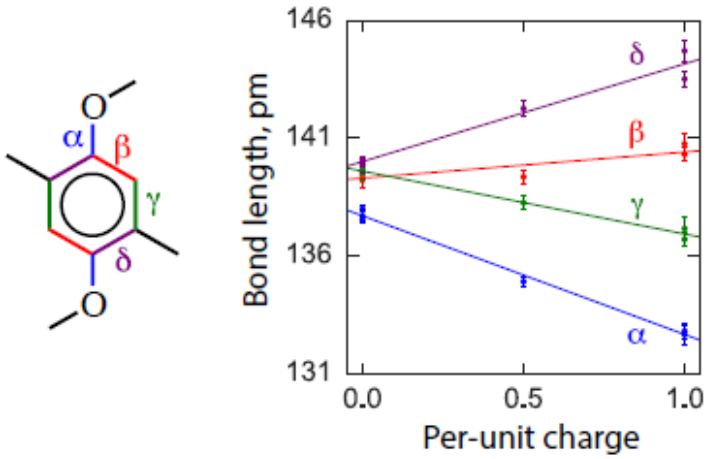

Figure S14. Bond lengths from various crystal structures of *p*-HE derivatives plotted against charge at their respective *p*-HE unit.

It is noteworthy that the magnitude of these bond length changes also varies for different bonds. For example, aromatic C-C bonds 'β'and 'γ' are somewhat insensitive to the amount of the charge at *p*-HE unit, while C_{Ar}-O bond 'α' and C-C bond 'δ' display high sensitivity to the amount of charge (Figure S15). Therefore, oxidation-induced change of a single bond (e.g. C_{Ar}-O bond) can serve as a reliable indicator of the oxidation state of the entire aryl group. Nevertheless, a simultaneous analysis of the all bond length changes provides a statistically significant picture about the spin/charge distribution in the oxidized aromatic hydrocarbons and will be referred to hereafter as global analysis.

*[**Pil**$_{1.5+\bullet}$ ($SbCl_6^-$)$_{1.5}$] crystal structure*

We have obtained two crystal structures of [**Pil**$_{1.5+\bullet}$ ($SbCl_6^-$)$_{1.5}$] with highly unusual stoichiometry, where each pillarene moiety was associated with 1.5 equivalents of an $SbCl_6^-$ counteranion, indicating that it bears 1.5 positive charges. Despite a varied precision of these structures (i.e., averaged uncertainties are 0.54 and 1.82 pm), the arrangement of pillarene molecules and $SbCl_6^-$ counter-anion in a unit cell as well as the overall packing are almost indistinguishable.

The [**Pil**$_{1.5+\bullet}$ ($SbCl_6^-$)$_{1.5}$] crystal structures shows that each pillarene molecule is involved in the formation of three dimeric contacts with sandwich-like arrangements of two *p*-HEs from adjacent pillarenes, identified as ***a***, ***b*** and ***c*** (Figure S16A). Inspection of these sandwich-like pairs shows that each pair has an interplanar separation of ~3.3 A, which is shorter than the sum of the van der Waals radii, suggesting that each pair can stabilize a single cationic charge similarly to other cyclophanelike donors. As shown above, aryl moieties in [**DAE**$^{+\bullet}$ $SbCl_6^-$] structure make parallel sandwiches with the interplanar separation of ~3.4 A and the slippage of ~2.8 A (Figure S16B) and they share a single cationic charge as established detailed global analysis of oxidation-induced bond length changes in Figures13-14. Therefore, a similar global analysis of the X-ray structures of [**Pil**$_{1.5+\bullet}$ ($SbCl_6^-$)$_{1.5}$] demonstrate that three *p*-HEs (i.e., units ***a***, ***b*** and ***c***) bear 0.5 charge and account for the formal 1.5 charge per pillarene while the other two *p*-HE rings (d and e) bear no charge. The details of this global analysis are presented below:

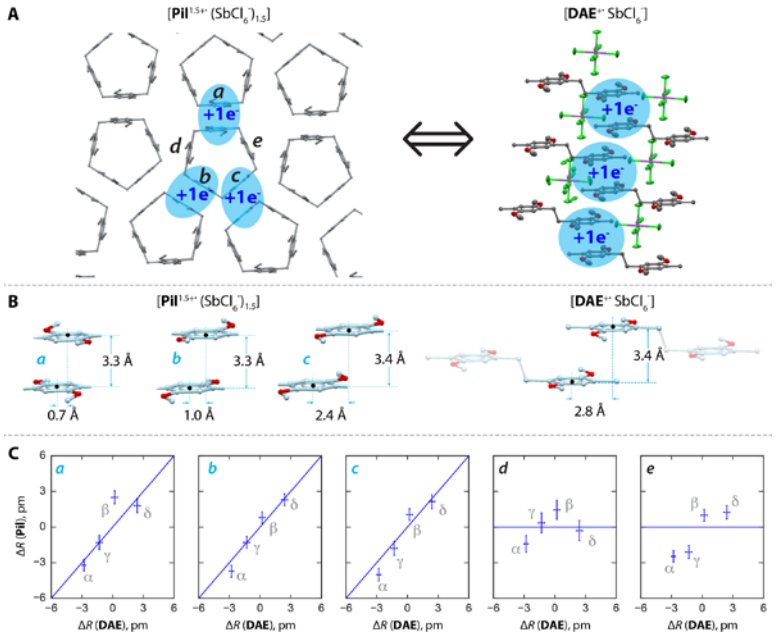

Figure S15. Top: Packing of [**Pil**$_{1.5+\bullet}$(SbCl$_6^-$)$_{1.5}$] and [**DAE**$_{+\bullet}$SbCl$_6^-$] crystal structures. Bottom: Plots of oxidation induced bond length changes in each unit of pillarene against bond length changes in **DAE**. Uncertainties (σ) of individual bond length changes are shown as error bars.

Analysis of the oxidation-induced bond length changes in each *p*-HE in [**Pil**$_{1.5+\bullet}$(SbCl$_6^-$)$_{1.5}$] shows that those units that are involved in the dimeric contacts (i.e., units ***a***, ***b***, and ***c***) undergo structural reorganization that is nearly identical to that found in the *p*-HE rings in **DAE**$_{+\bullet}$ (Table S4). Indeed, the correlation plots between oxidation-induced bond length changes in each *p*-HE in **Pil**$_{1.5+\bullet}$ and *p*-HEs in **DAE**$_{+\bullet}$ is linear with unity slopes for units ***a***, ***b***, and ***c***, while no correlation exists for *p*-HEs that are not involved in the dimeric contacts, i.e., units ***d*** and ***e*** (Figure S16C).

Table S4. Comparison of the bond lengths, their oxidation induced changes and their uncertainties (pm) in each *p*-HE unit in [**Pil**$_{1.5+\bullet}$(SbCl$_6^-$)$_{1.5}$] (raj28b5). Equivalent bonds are averaged.

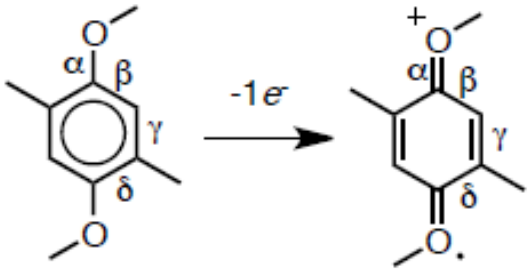

	α	β	γ	δ
Pil	138.2(1)	138.8(1)	139.1(1)	139.1(1)
a	135.0(5)	141.3(6)	137.8(6)	140.9(6)
b	135.5(5)	139.6(5)	137.8(5)	141.4(5)
c	134.2(6)	139.9(5)	137.3(5)	141.3(6)
d	136.8(7)	140.3(8)	139.5(9)	138.8(9)
e	135.8(5)	139.8(5)	137.0(6)	140.4(6)
ΔR (a)	-3.2(5)	2.5(6)	-1.3(6)	1.8(6)

ΔR (b)	-3.7(5)	0.8(5)	-1.3(5)	2.3(5)
ΔR (c)	-4.0(6)	1.1(5)	-1.8(6)	2.1(6)
ΔR (d)	-1.4(7)	1.5(8)	0.4(9)	-0.3(9)
ΔR (e)	-2.5(5)	1.0(5)	-2.1(6)	1.2(6)
ΔR (**DMX**)	-5.2(3)	0.9(3)	-2.9(3)	3.4(3)
ΔR (**DAP**)	-4.9(4)	1.2(4)	-2.5(5)	4.8(5)
ΔR (**DAE**)	-2.8(2)	0.2(3)	-1.3(3)	2.4(3)

A similar comparison with the oxidation-induced bond length changes in **DMX**$_{+\bullet}$ and **DAP**$_{2+}$, where aryl moieties bear a full cationic charge, shows that the oxidation-induced bond length changes in each *p*-HE in **Pil**$_{1.5+\bullet}$ are by factor of two smaller than those in found in **DMX**$_{+\bullet}$ and **DAP**$_{2+}$ (Table S4). Indeed, correlation plots between oxidation-induced bond length changes in each *p*-HE in **Pil**$_{1.5+\bullet}$ and *p*-HEs in **DMX**$_{+\bullet}$ (or **DAP**$_{2+}$) has a linear slope of 0.5 for units ***a***, ***b***, and ***c***, while no correlation were found *p*-HEs units ***d*** and ***e*** (Figure S17, S18).

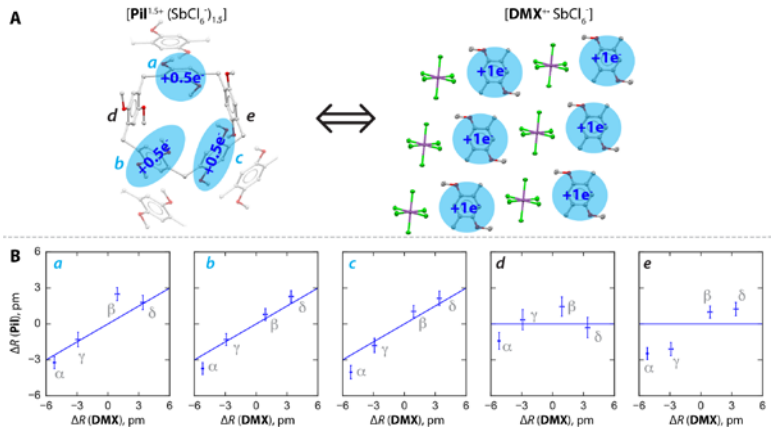

Figure S16. Top: Packing of [**Pil**$_{1.5+\bullet}$ (SbCl$_{6-}$)$_{1.5}$] and [**DMX**$_{+\bullet}$ SbCl$_{6-}$] crystal structures. Bottom: Plots of oxidation induced bond length changes in each unit of pillarene against bond length changes in **DMX**. Uncertainties (σ) of individual bond length changes are shown as error bars.

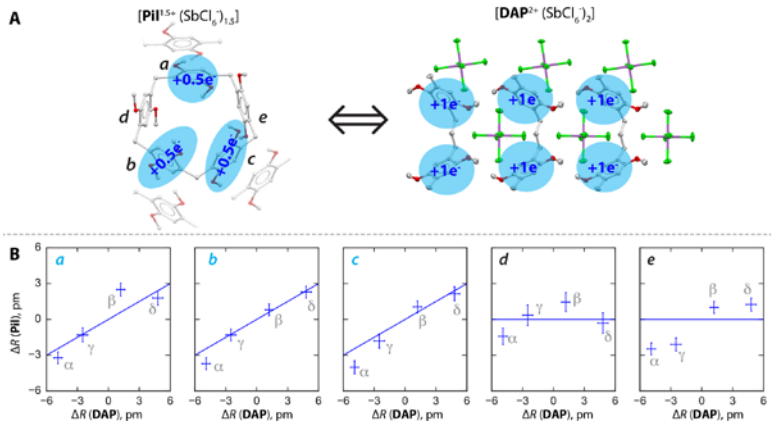

Figure S17. Top: Packing of [**Pil**$_{1.5+\bullet}$ (SbCl$_{6-}$)$_{1.5}$] and [**DAP**$_{2+}$(SbCl$_{6-}$)$_2$] crystal structures. Bottom: Plots of oxidation induced bond length changes in each unit of pillarene against bond length changes in **DAP**. Uncertainties (σ) of individual bond length changes are shown as error bars.

An analysis of the second (less precise) structure of [**Pil**$_{1.5+\bullet}$ (SbCl$_{6-}$)$_{1.5}$] showed a similar distribution of the bond length changes in *p*-HE rings **a**, **b**, **c**, **d**, and **e**. As compared to the first structure, second structure has a lower

precision (1.82 pm vs 0.54) and only a few of the bond-length changes satisfy 3σ confidence level (Table S19), yet a cumulative analysis of the bond-length changes and their comparison with the model compounds **DAE**$_{+\bullet}$, **DMX**$_{+\bullet}$ and **DAP**$_{2+}$ clearly indicates that units ***a***, ***b***, and ***c*** bear ~0.5 charge, while units ***d*** and ***e*** are uncharged (Figure S19).

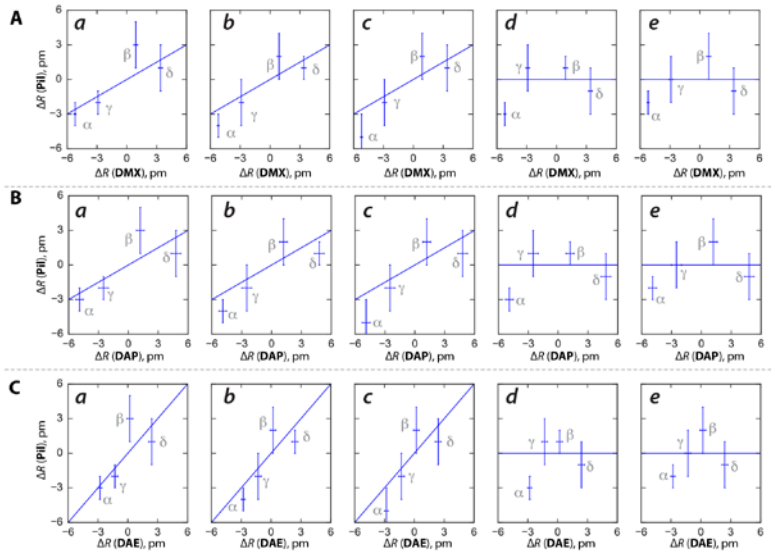

Figure S18. Plots of oxidation induced bond length changes in each unit of pillarene against bond length changes in **DMX**, **DAP** and **DAE**. Uncertainties (σ) of individual bond length changes are shown as error bars.

Table S5. Comparison of the bond lengths, their oxidation induced changes and their uncertainties (pm) in each *p*-HE unit in [**Pil**$_{1.5+\bullet}$(SbCl$_{6-}$)$_{1.5}$] (raj13ka). Equivalent bonds are averaged.

	α	β	γ	δ
Pil	138.2(1)	138.8(1)	139.1(1)	139.1(1)
a	135(1)	142(2)	138(1)	141(2)
b	135(1)	141(2)	138(2)	140(2)
c	134(2)	141(2)	137(2)	141(2)
d	136(1)	140(1)	140(2)	139(2)
e	137(1)	141(2)	139(2)	139(2)
ΔR (a)	-3(1)	3(2)	-2(1)	1(2)
ΔR (b)	-4(1)	2(2)	-2(2)	1(2)
ΔR (c)	-5(2)	2(2)	-2(2)	1(2)
ΔR (d)	-3(1)	1(1)	1(2)	-1(2)
ΔR (e)	-2(1)	2(2)	0(2)	-1(2)
ΔR (**DMX**)	-5.2(3)	0.9(3)	-2.9(3)	3.4(3)
ΔR (**DAP**)	-4.9(4)	1.2(4)	-2.5(5)	4.8(5)
ΔR (**DAE**)	-2.8(2)	0.2(3)	-1.3(3)	2.4(3)

ELECTRONIC STRUCTURE OF PILLARENE IN SOLUTION

Computational details

The electronic structure calculations were performed using B1LYP-40/6-31G(d)[16,17] level of theory[18-22] as implemented in Gaussian 09 package, revision D.01.[23] Solvent effects were included using the implicit integral equation formalism polarizable continuum model (PCM)[24-28] with dichloromethane as a solvent. Ultrafine Lebedev's grid was used for all calculations. Tight convergence criteria were used in geometry optimization

procedures. Harmonic vibrational frequency calculations were performed to confirm absence of imaginary frequencies. For **DMX**$^{+\bullet}$ and **Pil**$^{+\bullet}$, wavefunction stability test[29] was performed to ensure absence of solutions with lower energy. The value of $\langle S_2 \rangle$ after spin annihilation was confirmed to be close to the expected value of 0.75.

*DFT calculations of **Pil**$^{+\bullet}$*

In neutral pillarene (**Pil**), HOMO is delocalized over the entire molecule (Figure S19). In pillarene cation radical (**Pil**$^{+\bullet}$), spin-density distribution is limited to a single *p*-HE ring (Figure S19), which agrees with the negligible change in the oxidation energy of **Pil** as compared to the model compound (**DMX**), i.e. E_{ox1}(**DMX**) = 5.143 eV vs. E_{ox1}(**Pil**) = 5.096 eV – a difference of 47 meV. Notably, the spin/charge distribution in **Pil**$^{+\bullet}$ is accompanied by the structural reorganization, which occurs in the form of quinoidal distortion of a single *p*-HE unit. This involves a shortening of the C-O bonds (by ~5 pm), lengthening/contractions (by ~1-4 pm) of the equivalent aromatic C-C bonds, as shown in Figure S20 and Table S6. Also see below the discussion concerning the hole delocalization amongst the *p*-HE rings (which can be artificially modulated by varying the % HF)[12] based on the *application of the Marcus-based multistate model to **Pil**$^{+\bullet}$.*

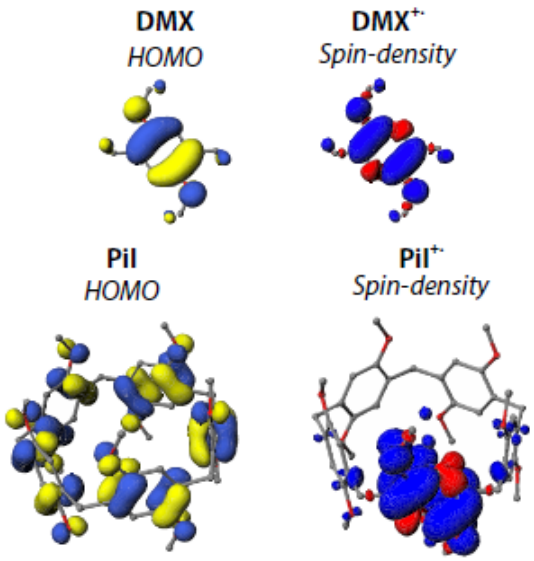

Figure S19. Isovalue plots of HOMOs and spin-densities of pillarene (**Pil**) and its model compound (**DMX**).

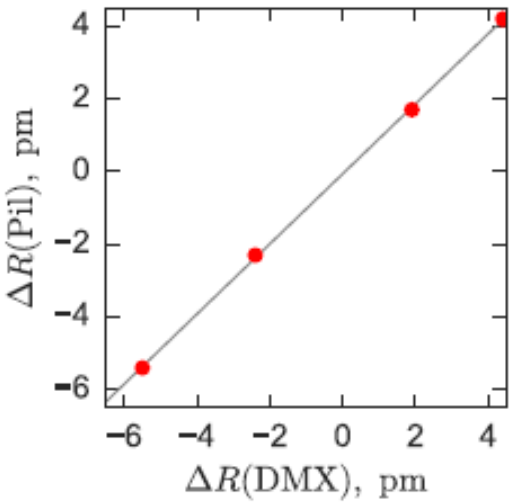

Figure S20. Plot of the oxidation-induced bond lengths in **DMX**/**DMX**$^{+\bullet}$ and **Pil**/**Pil**$^{+\bullet}$ computed at B1LYP-40/6-31G(d)+PCM(CH_2Cl_2).

Table S6. Comparison of the oxidation-induced bond lengths in **DMX**/**DMX**$^{+\bullet}$ and a single *p*-HE unit (where the most of the charge resides, see Figure S19) of **Pil**/**Pil**$^{+\bullet}$ computed at B1LYP-40/6-31G(d)+PCM(CH_2Cl_2).

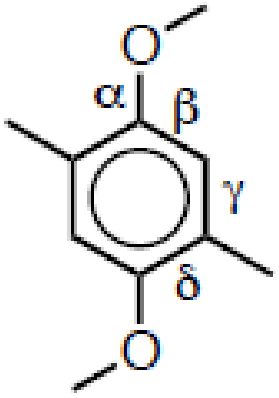

	Pil$^{+\bullet}$	**Pil**	Δ*R*, pm	**DMX**$^{+\bullet}$	**DMX**	Δ*R*, pm
α	1.314	1.368	-5.4	1.310	1.365	-5.5
β	1.409	1.392	1.7	1.411	1.392	1.9
γ	1.369	1.392	-2.3	1.368	1.392	-2.4
δ	1.440	1.398	4.2	1.441	1.397	4.4

Application of the Marcus-based multistate model to ***Pil***$^{+\bullet}$

Oxidation of the *p*-HE unit in **Pil**$^{+\bullet}$ with coordinate x_i leads to the structural reorganization of this unit and accumulation of the negative charge due to the solvation. Fixing the geometry of the reorganized unit, a variation of the reaction coordinate *x* unit leads to the energy increase that can be described using quadratic approximation in the short-range, while at a larger separation distance the energy reaches a finite value following the inverse dependence according to Coulomb law of the electrostatic interaction.[30] Thus, each diabatic state can be represented as a bell-shaped function $H_i(x)$ of the charge coordinate x using the composite quadratic/reciprocal function:[30]

$$H_i(x) = \begin{cases} \lambda(x - x_i)^2, if\ |x - x_i| \le t \\ \lambda^{\infty} - a/|x - x_i|, if\ |x - x_i| \ge t \end{cases}$$

where λ is the structural reorganization, λ^{∞} is the energy of the completely separated hole and reorganization, parameters $t = \sqrt{\lambda^{\infty}/3\lambda}$ and $a = 2\lambda t^3$ are defined by the continuity of $H_i(x)$ and its first derivative. Due to the circular topology of pillarene molecule, there is an off-diagonal element in the Hamiltonian matrix, while $H_i(x)$ must satisfy the periodic boundary conditions. The Hamiltonian matrix can be represented as (also see Ref.[31] for details):

$$\mathbf{H}(x) = \begin{bmatrix} H_1(x) & H_{ab} & \dots & 0 & H_{ab} \\ H_{ab} & H_2(x) & \cdots & 0 & 0 \\ \vdots & \vdots & \ddots & \vdots & \vdots \\ 0 & 0 & \cdots & H_{n-1}(x) & H_{ab} \\ H_{ab} & 0 & \cdots & H_{ab} & H_n(x) \end{bmatrix}$$

Hamiltonian matrices at various *x* were constructed using values $H_{ab} = 0.08eV$ (taken as the value of β obtained from the Huckel method, see Figure 7A in the manuscript) and $\lambda = 0.74\ eV$ and $\lambda^{\infty} = 1.5\ eV$ obtained from our previous studies on molecular wires consisting from *p*-HE units.[32] Numerical diagonalization of the Hamiltonian matrix $\mathbf{H}\ x$ for each x results in the adiabatic potential energy surface (PES) with the lowest-energy surface $G_0(x)$ corresponding to the ground state of **Pil**$^{+\bullet}$ (Figure S21). The PES of **Pil**$^{+\bullet}$ has five minima that

correspond to charge localized at one of the *p*-HE units with the interconversion barrier of 0.12 eV (2.7 kcal/mol). Due to the small electronic coupling and large reorganization energy MSM shows that ~98% of the charge is localized on a single *p*-HE unit.

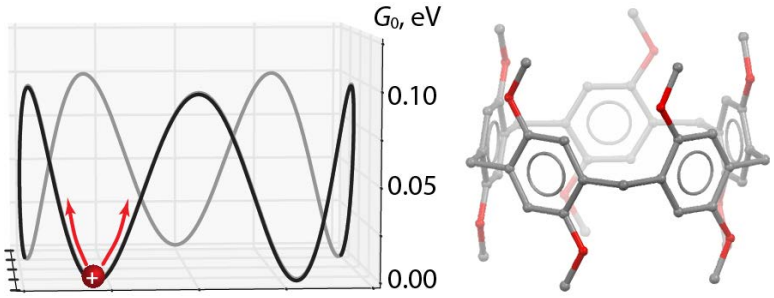

Figure S21. Potential energy surface of obtained from MSM**.**

REFERENCES

[1] M. R. Talipov, A. Boddeda, M. M. Hossain, R. Rathore, *J. Phys. Org. Chem.* **2015**, *29*, 227-233.
[2] M. R. Talipov, M. M. Hossain, A. Boddeda, K. Thakur, R. Rathore, *Org. Biomol. Chem.* **2016**, *14*, 2961-2968.
[3] R. Rathore, J. K. Kochi, *J. Org. Chem.* **1995**, *60*, 4399-4411.
[4] T. Ogoshi, S. Kanai, S. Fujinami, T. -A. Yamagishi, Y. Nakamoto, *J. Am. Chem. Soc.* **2008**, *130*, 5022-5023.
[5] C. Han, F. Ma, Z. Zhang, B. Xia, Y. Yu, F. Huang, *Org. Lett.* **2010**, *12*, 4360-4363.
[6] P. J. Cragg, K. Sharma, *Chem. Soc. Rev.* **2012**, *41*, 597-607.
[7] C. R. Groom, I. J. Bruno, M. P. Lightfoot, S. C. Ward, *Acta. Crystallogr. B. Struct. Sci. Cryst. Eng.Mater.* **2016**, *72*, 171-179.
[8] T. S. Navale, K. Thakur, V. S. Vyas, S. H. Wadumethrige, R. Shukla, S. V. Lindeman, R. Rathore, *Langmuir.* **2012**, *28*, 71-83.
[9] T. S. Navale, M. R. Talipov, R. Shukla, R. Rathore, *J. Phys. Chem. C.* **2016**, *120*, 19558-19565.
[10] D. Sun, S. V. Lindeman, R. Rathore, J. K. Kochi, *J. Chem. Soc. Perkin. Trans. 2.* **2001**, 1585-1594.
[11] M. R. Talipov, T. S. Navale, R. Rathore, *Angew. Chem. Int. Ed.* **2015**, *54*, 14468-14472.
[12] M. R. Talipov, A. Boddeda, Q. K. Timerghazin, R. Rathore, *J. Phys. Chem. C.* **2014**, *118*, 21400-21408.
[13] M. V. Ivanov, K. Thakur, A. Bhatnagar, R. Rathore, *Chem. Commun. (Camb).* **2017**, *53*, 2748-2751.
[14] M. V. Ivanov, K. Thakur, A. Boddeda, D. Wang, R. Rathore, *J. Phys. Chem. C.* **2017**, *121*, 9202-9208.
[15] D. Wang, M. R. Talipov, M. V. Ivanov, R. Rathore, *J. Am. Chem. Soc.* **2016**, *138*, 16337-16344.
[16] W. J. Hehre, R. Ditchfield, J. A. Pople, *J. Chem. Phys.* **1972**, *56*, 2257-2261.
[17] C. Adamo, V. Barone, *Chem. Phys. Lett.* **1997**, *274*, 242-250.
[18] M. Felix, A. A. Voityuk, *Int. J. Quantum. Chem.* **2011**, *111*, 191-201.
[19] M. Dierksen, S. Grimme, *J. Phys. Chem. A.* **2004**, *108*, 10225-10237.
[20] M. R. Talipov, A. Boddeda, Q. K. Timerghazin, R. Rathore, *J. Phys. Chem. C.* **2014**, *118*, 21400-21408.
[21] A. J. Cohen, P. Mori-Sanchez, W. Yang, *Chem. Rev.* **2011**, *112*, 289-320.
[22] A. J. Cohen, P. Mori-Sanchez, W. Yang, *Science.* **2008**, *321*, 792-794.
[23] Frisch, M. J.; Trucks, G. W.; Schlegel, H. B.; Scuseria, G. E.; Robb, M. A.; Cheeseman, J. R.; Scalmani, G.; Barone, V.; Mennucci, B.; Petersson, G. A.; Nakatsuji, H.; Caricato, M.; Li, X.; Hratchian, H. P.; Izmaylov, A. F.; Bloino, J.; Zheng, G.; Sonnenberg, J. L.; Hada, M.; Ehara, M.; Toyota, K.; Fukuda, R.; Hasegawa, J.; Ishida, M.; Nakajima, T.; Honda, Y.; Kitao, O.; Nakai, H.; Vreven, T.; Montgomery, J. A.; Peralta, J. E.; Ogliaro, F.; Bearpark, M.; Heyd, J. J.; Brothers, E.; Kudin, K. N.; Staroverov, V. N.; Kobayashi, R.; Normand, J.; Raghavachari, K.; Rendell, A.; Burant, J. C.; Iyengar, S. S.; Tomasi, J.; Cossi, M.; Rega, N.; Millam, J. M.; Klene, M.; Knox, J. E.; Cross, J. B.; Bakken, V.; Adamo, C.; Jaramillo, J.; Gomperts, R.; Stratmann, R. E.; Yazyev, O.; Austin, A. J.; Cammi, R.; Pomelli, C.; Ochterski, J. W.; Martin, R. L.; Morokuma, K.; Zakrzewski, V. G.; Voth, G. A.; Salvador, P.; Dannenberg, J. J.; Dapprich, S.; Daniels, A. D.; Farkas; Foresman, J. B.; Ortiz, J. V.; Cioslowski, J.; Fox, D. J. Gaussian, Inc., Wallingford CT, 2009. [24] J. Tomasi, B. Mennucci, R. Cammi, *Chem. Rev.* **2005**, *105*, 2999-3094.

[25] S. Miertus, E. Scrocco, J. Tomasi, *Chem. Phys.* **1981**, *55*, 117-129.
[26] M. Cossi, V. Barone, B. Mennucci, J. Tomasi, *Chem. Phys. Lett.* **1998**, *286*, 253-260.
[27] E. Cances, B. Mennucci, J. Tomasi, *J. Chem. Phys.* **1997**, *107*, 3032-3041.
[28] R. F. Ribeiro, A. V. Marenich, C. J. Cramer, D. G. Truhlar, *J. Phys. Chem. B.* **2011**, *115*, 14556-14562.
[29] R. Bauernschmitt, R. Ahlrichs, *J. Chem. Phys.* **1996**, *104*, 9047-9052.
[30] M. R. Talipov, M. V. Ivanov, R. Rathore, *J. Phys. Chem. C.* **2016**, *120*, 6402-6408.
[31] M. R. Talipov, R. Jasti, R. Rathore, *J. Am. Chem. Soc.* **2015**, *137*, 14999-15006.
[32] M. V. Ivanov, V. J. Chebny, M. R. Talipov, R. Rathore, *J. Am. Chem. Soc.* **2017**, *139*, 4334-4337.

References

1 Ballauff, M., *Science* 2016, **352**, 656– 657.
2 Kory, M. J., Wörle, M., Weber, T., Payamyar, P., van de Poll, S. W., Dshemuchadse, J., Trapp, N.,Schlüter, A. D., *Nat. Chem.* 2014, **6**, 779– 784.
3 Zhuang, X., Mai, Y., Wu, D., Zhang, F., Feng, X., *Adv. Mater.* 2015, **27**, 403– 427.
4 Navale, T. S., Thakur, K., Vyas, V. S., Wadumethrige, S. H., Shukla, R., Lindeman, S. V., Rathore, R., *Langmuir* 2012, **28**, 71– 83.
5 Brédas, J.-L., Beljonne, D., Coropceanu, V., Cornil, J., *Chem. Rev.* 2004, **104**, 4971– 5004.
6 Li, C., Liu, M., Pschirer, N. G., Baumgarten, M., Müllen, K., *Chem. Rev.* 2010, **110**, 6817– 6855.
7 Talipov, M. R., Jasti, R., Rathore, R., *J. Am. Chem. Soc.* 2015, **137**, 14999– 15006.
8 Ivanov, M. V., Chebny, V. J., Talipov, M. R., Rathore, R., *J. Am. Chem. Soc.* 2017, **139**, 4334– 4337.
9 Ogoshi, T., Kanai, S., Fujinami, S., Yamagishi, T.-A., Nakamoto, Y., *J. Am. Chem. Soc.* 2008, **130**,5022– 5023.
10 Cragg, P. J., Sharma, K., *Chem. Soc. Rev.* 2012, **41**, 597– 607.
11 Strutt, N. L., Zhang, H., Schneebeli, S. T., Stoddart, J. F., *Acc. Chem. Res.* 2014, **47**, 2631– 2642.
12 Liu, Z., Nalluri, S. K. M., Stoddart, J. F., *Chem. Soc. Rev.* 2017, **46**, 2459– 2478.
13 Rathore, R., Kochi, J. K., *J. Org. Chem.* 1995, **60**, 7479– 7490.
14 Geiger, W. E., Barrière, F., *Acc. Chem. Res.* 2010, **43**, 1030– 1039.
15 Ivanov, M. V., Talipov, M. R., Boddeda, A., Abdelwahed, S. H., Rathore, R., *J. Phys. Chem. C* 2017,**121**, 1552– 1561.
16 Navale, T. S., Talipov, M. R., Shukla, R., Rathore, R., *J. Phys. Chem. C* 2016, **120**, 19558– 19565.
17 Rathore, R., Burns, C. L., Deselnicu, M. I., *Org. Synth.* 2005, 1– 9.
18 Talipov, M. R., Boddeda, A., Hossain, M. M., Rathore, R., *J. Phys. Org. Chem.* 2016, **29**, 227– 233.
19 Tsuchida, A., Tsujii, Y., Ohoka, M., Yamamoto, M., *J. Phys. Chem.* 1991, **95**, 5797– 5802.
20 Badger, B., Brocklehurst, B., *Trans. Faraday. Soc.* 1970, **66**, 2939– 2947.
21 Demadis, K. D., Hartshorn, C. M., Meyer, T. J., *Chem. Rev.* 2001, **101**, 2655– 2686.
22 Li, G., Govind, N., Ratner, M. A., Cramer, C. J., Gagliardi, L., *J. Phys. Chem. Lett.* 2015, **6**, 4889– 4897.
23 Lambert, C., Nöll, G., Schelter, J., *Nat. Mater.* 2002, **1**, 69– 73.
24 Rathore, R., Lindeman, S. V., Kumar, A. S., Kochi, J. K., *J. Am. Chem. Soc.* 1998, **120**, 6931– 6939.
25 Han, C., Ma, F., Zhang, Z., Xia, B., Yu, Y., Huang, F., *Org. Lett.* 2010, **12**, 4360– 4363.
26 Groom, C. R., Bruno, I. J., Lightfoot, M. P., Ward, S. C., *Acta Crystallogr. Sect. B* 2016, **72**, 171– 179.
27Largely neutral **d** and **e** *p*-HE units lie relatively close with *p*-HEs from other pillarenes, however such dimers exist exclusively in a non-parallel “staggered” conformation.
28 Wartini, A. R., Valenzuela, J., Staab, H. A., Neugebauer, F. A., *Eur. J. Org. Chem.* 1998, 139– 148.
29 Sun, D., Lindeman, S. V., Rathore, R., Kochi, J. K., *J. Chem. Soc. Perkin Trans. 2* 2001, 1585– 1594.
30 Talipov, M. R., Navale, T. S., Rathore, R., *Angew. Chem. Int. Ed.* 2015, **54**, 14468– 14472; *Angew. Chem.* 2015, **127**, 14676– 14680.
31 Borden, W. T. in *Modern molecular orbital theory for organic chemists*, Prentice-Hall Englewood Cliffs, New Jersey, 1975.
32 Frost, A. A., Musulin, B., *J. Chem. Phys.* 1953, **21**, 572– 573.
33 Talipov, M. R., Boddeda, A., Timerghazin, Q. K., Rathore, R., *J. Phys. Chem. C* 2014, **118**, 21400– 21408.

34Intermolecular electronic coupling (β) between a pair of *p*-HE rings in a an idealized dimer was computed [B1LYP-40/6–31G(d)+PCM(CH2Cl2)] to be 340 meV.

35 Reilly, N., Ivanov, M., Uhler, B., Talipov, M., Rathore, R., Reid, S. A., *J. Phys. Chem. Lett.* 2016, **7**,3042– 3045.